Electrospun YMn$_2$O$_5$ nanofibers: A highly catalytic activity for NO oxidation

Tong Zhang[a,1], Hui Li[a,1], Zhi Yang[a], Fengren Cao[b], Liang Li[b], Haijun Chen[a], Hui Liu[a], Ka Xiong[c], Jie Wu[d], Zhanglian Hong[e], Weichao Wang[a,f,*]

[a] Department of Electronics and Tianjin Key Laboratory of Photo-Electronic Thin Film Device and Technology, National Institute for Advanced Materials, Nankai University, Tianjin, 300071, China
[b] College of Physics, Optoelectronics and Energy, Center for Energy Conversion Materials & Physics (CECMP), Jiangsu Key Laboratory of Thin Films, Soochow University, Suzhou 215006, China
[c] Dongguan Innovative New Materials Co. Ltd, Dongguan 523000, China
[d] College of material Science and Engineering, Shandong University of Science and Technology, Qingdao 266590, China
[e] State Key Laboratory of Silicon Materials, School of Materials Science and Engineering, Zhejiang University, No. 38 Zheda Road, Hangzhou 310027, China
[f] Department of Materials Science & Engineering, The University of Texas at Dallas, Richardson, TX 75252, USA

ARTICLE INFO

ABSTRACT

Nanofiber catalysts are potentially promising to be equipped in the lean-burned vehicle exhaust emission system considering its facile synthesis, low-cost, long durability in contrast to the traditionally complicated powder based catalyst. Here, via electrospinning method, we synthesized YMn$_2$O$_5$ nanofibers (average diameter: ˜93 nm) including nanowire stacked with particles, and hollow tubes with or without inside nanowires. The morphologies remained even after hydrothermal aging at 800 ℃ for 10 h with 10% H$_2$O stream. X-ray photoelectron spectrum revealed Mn^{4+}/Mn^{3+} ratio 0.589 on the surface of YMn$_2$O$_5$ catalyst (YMO), indicating the existence of oxygen vacancies. The highest conversion of electrospun mullite fibers at 310 ℃ is ˜18% higher than powder-based YMO at 352 ℃ in the presence of 5% H$_2$O at WHSV = 240,000 ml g^{-1} h^{-1}. The extracted activation energy from NO-to-NO$_2$ conversion curves of YMO nanofiber (61.68 kJ/mol) is slightly lower than that of powder-based mullite (91.45 kJ/mol), consistent with calculated 68.16 kJ/mol on the fiber YMO surface (121) with a rate-limiting step of the NO$_2$ desorption. The catalytic activity can be attributed to the unit occupy of the e_g (d_z^2 and $d_{x-y}^{2\,2}$) orbitals of Mn-dimer atoms around fermi level based on the combination of the theoretical calculations and DRIFTS spectra analysis. Importantly, after the hash hydrothermal-aging, the highest NO oxidation conversion of powder-based mullite is less than 50%, while the fiber maintains a conversion of 62%. Moreover, the fresh YMO fiber maintained superior oxidation stability for 12 h at its maximum conversion of 66%. This work provides the possibility for mullite oxide fibers to replace powder-based precious metal catalyst coating on monolith converter.

1. Introduction

Diesel engines possess higher fuel efficiency owing to its higher air/fuel ratio than the gasoline counterpart. However, resulting from the lean burn condition, diesel engine emits more NO$_x$ pollutants, refereeing to NO and NO$_2$ but mainly NO. NO$_x$ could cause a seriously detrimental effect on human health and environment when the concentration exceeds 0.05 ppm in the air. Ammonia selective catalytic reduction (NH$_3$-SCR) and NO$_x$ storage and reduction (NSR) are current important technologies to remove the pollutant NO$_x$ (deNO$_x$) [1–3]. Increasing the ratio of NO$_2$ in the exhaust gas of lean-burning vehicles helps to improve the low-temperature activity of the fast selective catalytic reduction (fast-SCR) catalyst [4], the adsorption performance of the storage reduction (NSR) catalyst, and promote the continuous regeneration of the diesel particulate filter (DPF). It is thus important to design highly efficient catalyst to oxide NO into NO$_2$. In view of the above situation, precious metal (Pt, Pd, Ru, Rh) catalysts have been widely studied for NO oxidation to NO$_2$ owing to their high catalytic activity [5–9]. However, noble metal catalysts suffer from their high cost in the massive production. During the past decades, transition metal (Fe, V, Cr, Cu, Ce, Mn) oxides catalysts have been attracted much attention in terms of NO oxidation [1,4,10–15].

Fig. 1. (a) Crystal structure of YMn_2O_5 mullite. (b) XRD patterns of as-spun fibers and powder-based mullite before and after aging. SEM images of fiber sample (c) before aging, (d) after aging, and the diameters of fibers distribution are shown in the inset pictures.

The traditional way to equip the above-mentioned catalysts into the vehicle is to coat the powder catalysts into the monolith converter, which is widely used in today's vehicles. As a comparison, fiber catalysts could be simply loaded into the monolith converter and avoid the complicated coating process as shown in Fig. S1. Therefore, the development of fiber catalyst could be promising to provide an alternative way to refine the current powder-based coating technology. Electrospinning is one of the widely used techniques to synthesize the nanofibers, applying a high voltage between the tip and collector to create Taylor Cone to drive the polymer solution overcoming its surface tension and subsequently form the fibers in the collector [16,17]. To date, there has been some work reporting on the electrospun fabrication of the nanofiber catalysts for CO oxidation [18].

In this work, we propose a ternary mullite oxide YMn_2O_5 (YMO), belonging to the diamond crystal structure with a space group of Pbam [19,20]. MnO_5 square-pyramid units are linked by edge-shared MnO_6 octahedra polyhedrons (Fig. 1a). From our calculations, due to the coexistence of two crystal fields, Mn's 3d orbitals especially, $3d_z^2$ dominate the Fermi level region which leads to the catalytic performance of NO and CO oxidation [20,21]. Herein, we prepared mullite nanofibers catalyst YMn_2O_5 via electrospinning technique and subsequent calcination at 800 °C in the air for 4 h. The calcined nanofiber displays a high specific surface area (42.91 m^2/g) and the diameters vary from 80 to 120 nm. In the presence of harsh hydrothermal condition with 10% H_2O at 800 °C for 10 h, the mullite oxide nanofiber shows high thermal stability with morphological retaining well. Furthermore, during the reaction, 5% water vapor was introduced to simulate the real exhaust gas condition, and YMO fibers exhibited a NO conversion ~18% higher than powder-based YMO. This work demonstrates a superior catalytic performance of the YMO nanofiber rivaling the powder-based mullite catalyst.

2. Experimental

2.1. Materials

Manganese acetate tetrahydrate [$Mn(CH_3COO)_2\cdot4H_2O$] was supplied by Tianjin Guangfu fine chemical research institute. Potassium permanganate [$KMnO_4$] and sodium hydroxide [NaOH] were taken from Aladdin Corporation. Yttrium nitrate hexahydrate [$Y(NO_3)_3\cdot6H_2O$] was obtained from Acros Organics Technology Corporation. Polyvinylpyrrolidone [PVP, $M_w \approx 1,300,000$] was taken from Meilun Biological Technology Corporation. Commercial 1 wt.% Pt on γ-Al_2O_3 was purchased from Sigma Aldrich Industrial Corporation and this material was not further optimized. And ethanol was commercially obtained from Meryer Chemical Technology Corporation.

2.2. Synthesis of pure phase YMn_2O_5 nanofibers and powder catalysts

Pure phase mullite (YMn_2O_5) catalysts were prepared by electrospinning method followed by calcination in the air as shown in Fig. S2. $Mn(CH_3COO)_2\cdot4H_2O$ and $Y(NO_3)_3\cdot6H_2O$ were used as metal precursors. More specifically, electrospinning precursor was prepared by dissolving 1.83 g $Y(NO_3)_3\cdot6H_2O$ and 2.34 g $Mn(CH_3COO)_2\cdot4H_2O$ in a mixed solution of 20 ml deionized water and 18 ml ethanol. Then the mixture was stirred until completely dissolving. Appropriate amounts of PVP was subsequently added and the mixed solution was continuously stirred for 10 h at room temperature to obtain electrospinning precursor. The above solution was fed by a 10 ml plastic syringe pump at a rate of 0.05 mm/min. A piece of aluminum foil was placed 15 cm from the tip of the metallic needle to collect the nanofibers and a high-voltage of 14–16 kV was applied between the needle and the collector. At first, the as-spun nanofibers were dried in air at 80 °C for 10 h and then, calcined at 500 °C for 8 h in order to remove volatile components and PVP, followed by a second calcination step at 800 °C for 4 h in air. The heating rate of muffle furnace was set at 25 °C /h during all above

calcination processes. Finally, the catalysts of YMn$_2$O$_5$ nanofibers were formed after naturally cooling down to room temperature.

A pure phase of YMn$_2$O$_5$ powder was also synthesized via hydrothermal methods. Stoichiometric amounts of high-purity Y(NO$_3$)$_3$·6H$_2$O, KMnO$_4$ and Mn(CH$_3$COO)$_2$·4H$_2$O were added into 25 ml deionized water in a molar ratio of 5: 3: 7, and then stirred for 30 min. 5.3 ml of the NaOH solution at a concentration of 5 M was added dropwise to the precursor. After stirring evenly, the mixture was transferred to a 100 ml Teflon-lined stainless steel autoclave and filled 60% of the autoclave capacity. The prepared precursor was hydrothermally aged at 200 °C for 12 h, and naturally cooling down to room temperature. After the product was filtered and washed three times with 1% HNO$_3$ and deionized water, the desired powder based mullite was obtained by drying at 100 °C for 4 h.

For simplicity, electrospun YMn$_2$O$_5$ nanofibers, powder-based YMn$_2$O$_5$, and commercial precious Pt catalysts are denoted as YMO-NFs, YMO-NPs, and Pt-NPs, respectively. The YMO-NPs and Pt-NPs powder were pressed into a pellet and then crushed to select 80–100 mesh small particles.

2.3. Characterization

The crystalline phases of mullite catalysts was identified by powder X-ray diffraction (XRD) and recorded on a Ulitma IV diffractometer which was operated at 40 kV and 40 mA with Cu Kα radiation source (λ = 0.154056 nm) at room temperature by a step of 0.02 s^{-1} in 2θ range from 10° to 80°. The scanning electron microscopy (SEM) images of samples were graphed with a ZEISS MERLIN Compact apparatus. The morphology and phase structure of the catalysts was observed by Transmission Electron Microscopy (HR-TEM) on a JEOL JEM-2010FEF equipment using an acceleration voltage of 200 kV. The Brunauer-Emmett-Teller (BET) specific surface area and pore volume of different catalysts were analyzed by N$_2$ adsorption/desorption at 77 K using a Micromeritics Surface Aera analyzer. X-ray Photoelectron Spectroscopy (XPS) measurements were performed on a Thermo Scientific ESCALAB 250Xi electron spectrometer with an exciting source of AlKα (1486.6 eV) at room temperature. The all binding energies were calibrated by the internal C1s line of adventitious carbon at 284.8 eV.

H$_2$-TPR was performed in ALTAMIRA AMI-300 micro-reactor. Firstly, 50 mg sample was pretreated in a stream of 5% O$_2$/N$_2$ (100 ml min^{-1}) at 300 °C for 30 min and then cooled down to room temperature. Then the sample was heated to 800 °C °C at a rate of 5 °C °C /min under a flow of 5% H$_2$/Ar (50 ml/min). The variation of H$_2$ amount in outlet gasses was analyzed by an on-line THERMO Star mass spectrum.

O$_2$-TPD, NO-TPD, and CO$_2$-TPD were carried on ALTAMIRA AMI-300 micro-reactor, equipped with THERMO Star mass spectrum. The catalyst (50 mg) was loaded into a U-shaped quartz tube and sandwiched between two quartz wool layers. Prior to each TPD test, the sample was heated up to 400 °C for 30 min under a flow of N$_2$ (30 ml/min) to remove pollutants on the catalyst and then, naturally cooled down to 50 °C. For O$_2$-TPD, 30 ml/min of O$_2$ flow was fed to the reactor at 50 °C for 90 min, thereby allowing the catalyst to absorb enough oxygen on their surface. Then the gas was switched to the He flow at 70 ml/min in order to remove excess oxygen molecules out of the sample surface. After that, the temperature ramped up to 800 °C °C at a heating rate of 10 °C/min under the flowing He gas (30 ml/min) and kept the constant temperature for 30 min. In addition, for NO-TPD, the catalyst was saturated with NO/N$_2$ stream (30 ml/min) at 50 °C after pre-treatment step and then, kept for 90 min. Excess of NO was removed by a flow of He (70 ml/min). And then, the sample was heated under the flowing He gas (30 ml/min) up to 600 °C at a constant heating rate as O$_2$-TPD. And for CO$_2$-TPD, the sample was saturated with 2% CO$_2$/He stream (30 ml/min) at 50 °C for 90 min after pre-treatment step and then, kept again in a flow of He (70 ml/min) for 15 min to blow the baseline. Subsequently, the sample was heated from 50 °C to 700 °C at a rate of 10 °C/min under a flow of He (50 ml/min). The composition of

the outlet gas was online monitored by mass spectrum.

2.4. Catalytic activity measurement

The activity of catalysts for NO oxidation was performed in a lean condition in a fixed bed reactor. 200 mg catalyst was placed in the middle of quartz tube between two clogs of quartz wool with 8 mm internal diameter for *in-situ* analysis and the temperature was detected by a K-type thermocouple. The reactant gas atmosphere consists of 500 ppm NO, 5% H$_2$O, excess O$_2$ and balance with N$_2$ at a total gas flow of 800 ml min^{-1} as shown in Fig. S2, corresponding to the weight hourly space velocity of 240,000 ml g$_{cat}$$^{-1}$ hour^{-1}. The catalysts were heated up from room temperature to 400 °C at 10 °C /min in a quartz fixed-bed reactor. In this process, we set the instrument to record one point every 25 °C and each temperature point lasts for 30 min to achieve the reaction balance. The gas composition as a function of temperature was analyzed by Nicolet iS10 infrared spectrometer. The conversion of NO to NO$_2$ was defined as below:

$$NO\,conversion\,(\%) = \frac{NO_{inlet} - NO_{outlet}}{NO_{inlet}} \times 100\%$$

In order to evaluate the thermal stability of the catalyst, we carried out hydrothermal experiments on the YMO-NFs, YMO-NPs, and Pt-NPs. The conditions of hydrothermal aging include heating samples up to 800 °C for 10 h in an atmosphere of 10% H$_2$O stream with a total gas flow rate 500 ml/min. In addition, durability experiment was carried out in the quartz tube for 12 h at the conversion point which exhibits the highest catalytic activity.

2.5. Calculation of activation energy

The activation energy (E$_a$ E$_a$) of the tested samples was calculated via the Arrhenius equation:

$$\ln k = \ln A - \frac{E_a}{R} \cdot \frac{1}{T},$$

where k is the reaction rate constant, R is the molar gas constant, T is the thermodynamic temperature, and A is the pre-factor. For the reaction 2 NO+ O$_2$ → 2NO$_2$, NO oxidation kinetic test was performed within the conversion ratio below 20% and then, the reaction rate equation can be expressed as: r= kC^2 = $-\frac{dC}{dt}$ r= kC^2 = $-\frac{dC}{dt}$. Here, C is the concentration of reactant NO. The relationship between reaction rate constant and temperature can be obtained by integrating the above equations and combining with NO conversion as shown: kτ= $\frac{1}{C_\tau}$ − $\frac{1}{C_0}$ kτ= $\frac{1}{C_\tau}$ − $\frac{1}{C_0}$, where τ is the time of NO contract with the catalyst. Then, by plotting lnk versus 1/T, the slope $-\frac{E_a}{R}$ $-\frac{E_a}{R}$ and E$_a$ can be obtained.

2.6. The DRIFT study on NO oxidation

In situ diffuse reflectance infrared Fourier transform spectroscopy (DRIFTS) measurements were performed on a Tensor-27 FT-IR spectrometer (Bruker, Germany) in the range of 1000–2000 cm^{-1} at a spectral resolution of 4 cm^{-1} with 50 scans. Prior to each experiment, the catalysts were pretreated at 400 °C for 30 min with 10% O$_2$ in the DRIFTS cell to ensure that complete adsorption saturation occurred and then cooled to the desired temperature. The reaction chamber was purged with Ar for 30 min to remove any residue and the background spectrum was recorded at each temperature under Ar flow. Thereafter, 500 ppm NO was introduced into the cell to investigate the pre-absorbed O$_2$ reaction with NO until the reaction reaches equilibrium, subsequently, 10% O$_2$ was once again introduced for 30 min at a different temperature to observe changes in absorption peaks.

2.7. Theoretical calculations

The calculations were performed by density functional theory (DFT) [22] with Spin-polarized generalized gradient approximations with Perdew Burke Ernzerhof (GGA-PBE) form, as implemented in the VASP code [23–25]. Electron-ion interactions were handled with the projector augmented wave (PAW) approach [26]. The energy cutoff of 400 eV was employed on the plane wave basis. For the structural optimization, the force accuracy is 0.02 eV/Å while the converged energy criterion is 10^{-5} eV in the calculation of electronic properties. The Gaussian smearing scheme was adopted with a smearing width of 0.05 eV A vacuum with a thickness of at least 12 Å was adopted to avoid the spurious interactions between the slab images. The Monkhorst-Pack k-mesh of $3 \times 3 \times 4$ and $2 \times 1 \times 1$ were used for bulk and (121) slab surface, respectively. To check the validations of the calculations, we calculated the bulk electronic structures which are well agreement with the experimental results (Fig. S3) [27].

To avoid the periodic image interaction between the adsorbates, for the (121) slab model, the supercell (1×2) was adopted with size a = 12.47 Å and b = 18 Å. In order to obtain reliable slab configurations with enough atomic layers converged, several testing relaxation simulations were performed with the thickness 9.2 Å, 10.5 Å, and 11.3 Å, respectively, and the slab thickness was finally used with 11.3 Å [21]. The latter half of slabs were fixed for all the surface calculations. In addition, to obtain the transition states information, climbing image nudged elastic band (CI-NEB) method was used with a linear interpolation of seven intermediate images between the reactant and product structures [28,29]. The adsorption energy (E_{ads}) of molecules was calculated via the expression [30], $E_{ads} = E_A + E_C - E_{AC}$, where E_A and E_C represent the energies of adsorbent molecules and YMO catalysis, respectively, and E_{AC} is the total energy of the system with the absorbed CO or O_2.

3. Results and discussion

3.1. Structural characterization

YMn_2O_5 polyhedral network framework is composed of O and Mn ions, and Y ions locate in the hollow site surrounded by polyhedrons. Mn^{3+} and Mn^{4+} are centered in the MnO_5 pyramidal (Mn_{pyr}) and MnO_6 octahedral (Mn_{oct}), respectively (Fig. 1a). The pure phase of as-spun crystalline YMO-NFs and hydrothermal synthesized YMO-NPs were revealed by XRD (JCPDS No. 34–667), as shown in Fig. 1b. In the spectrum of the as-prepared sample, the impurity phase was not observed in both YMO-NFs and YMO-NPs. For the hydrothermally aged sample, the feature peaks become narrow, indicating the further growth of the nanocrystal.

In order to access the surface morphologies of the nanofiber and powder catalysts before and after hydrothermal aging, SEM measurement has been conducted in Fig. 1c, d, and Fig. S4. In the fresh SEM image, except for the main configures of the fibers with the diameter ˜93 nm, a small amount of belt-shape fibers was observed as well (Fig. 1c). Based on statistics of 100 fibers after sample aging, the average diameter tended to increase up to 98 nm. The basic reason for the size increase after aging could be related to the growth of the particle, assembling the fiber, at a high temperature. This assumption could be validated by more porosities in the aged fibers. In contrast to the increase of the diameter size, the specific surface area decreases from 42.91 m^2/g to 27.56 m^2/g as shown in Table 1, according to N_2 adsorption-desorption isotherms displayed in Fig. S5. In comparison with YMO-NFs, the fresh YMO-NPs exhibits a fine granular or small spherical shape. The small particles agglomerated after hydrothermal aging in 800 °C for 10 h with 10% H_2O as shown in Fig. S4. Correspondingly, the specific surface area reduces (Fresh: 29.47 m^2/g; Aged: 18.73 m^2/g).

Through the measurements of transmission electron microscopy, it

Table 1
Surface areas and diameters of YMn_2O_5 fibers and powder-based YMn_2O_5 with and without hydrothermal aging.

Sample	YMn_2O_5 nanofibers		YMn_2O_5 powder
	Fiber diameter (nm)	S_{BET} (m^2/g)	S_{BET} (m^2/g)
Fresh	93±10	42.91	29.47
After aging	98±10	27.56	18.73

was found that in different regions there are three types of morphologies of the fibers in Fig. 2a–c. Specifically, in Fig. 2a, the fiber is mainly composed of mullite oxide particles with the diameter varying from 32 nm to 54 nm; in other areas, a hollow tube-shaped fiber structure with or without inside mullite nanowire was observed in Fig. 2b and c, respectively. High-resolution TEM further confirms the pure phase of the synthesized fiber as the (121) surface spacing is 0.307 nm (Fig. 2d). The corresponding atomic structures information of the (121) surface are shown in Fig. 2i and j. The slab surface is mainly composed of two types Mn-dimers with different oxygen vacancy (V_O), i.e., the V_O tetrahedron linked to a square pyramid (Mn_{pyr}-Mn_{tet}) and octahedron (Mn_{oct}-Mn_{tet}), respectively, which might be vital to activate O_2 molecule. Here, it is worth to notice that the interesting tube structures in Fig. 2b and c, possibly resulting from the decomposition of the organic polymer during the sampling calcination. For the tubes without inside nanowire (Fig. 2b), the inner diameter is 46.7 nm and the wall thickness varies from 25 nm to 30 nm. This specific hollow nanostructure could potentially double the active sites since the reaction could happen on both sides of the tube. Interestingly, there exists a nanowire with diameter ˜32 nm in the tube in Fig. 2c, this specific structure could further increase the active sites since reactions also take place over the inside nanowire. Currently, these three types of morphologies coexist together in this work. For the future work, it would mean to refine the synthesis condition to fabricate uniform structure to further improve the catalytic performance.

Besides, the elemental composition of as-spun nanofibers was further characterized by STEM, elements of Y, Mn and O are evenly distributed in the nanofiber from the elemental mappings as shown in Fig. 2f–h. Under the electron microscope, the electrospun fiber resembles the thorn vine as shown in Fig. 2e. Along the tube Y, Mn, and O distributed uniformly. Importantly, various small particles located outside the tube. For each one, the mapping information suggests the particle mullite composition with the particle size ranging from 20 to 60 nm.

3.2. XPS valence state analysis

XPS measurement was carried out to obtain the surface chemical composition and the corresponding valence states of a catalyst. The survey spectra showed interference signals of Mn, O, and Y in the range of 0–800 eV (Fig. 3a). Through the analysis of Mn-2p spectra (Fig. 3b), it was found that Mn-2p peak was deconvoluted into two group peaks of Mn^{3+} (641.3–641.7 eV) and Mn^{4+} (642.2–643.3 eV) species [31–34]. The peak at 641.89 eV is attributed to Mn-2p$_{3/2}$. Due to the small different binding energies of Mn^{3+} and Mn^{4+}, the main spectra can be converted into two peaks at 641.5 eV and 643.2 eV corresponding to the Mn^{3+} and Mn^{4+} species, respectively. The Mn^{4+}/Mn^{3+} atomic ratio is 0.589 based on the integral of the peak areas. In the mullite crystalline, two ligand fields coexist, i.e., octahedron (Mn^{4+}) and pyramid (Mn^{3+}) [20,27]. Upon previous work, only in Mn^{3+}-centered pyramid, d_{z2} is occupied as the valence band maximum. For Mn^{4+}-centered octahedral, e_g orbital is empty. In other words, only Mn^{3+} sites could be effectively utilized during the catalytic reactions.

For the (121) surface exposed fiber materials, the large amount of Mn^{3+} corresponds to the O vacancy on the surface of the fiber catalysts (Fig. 2j). The total and projected density of states reveals that the
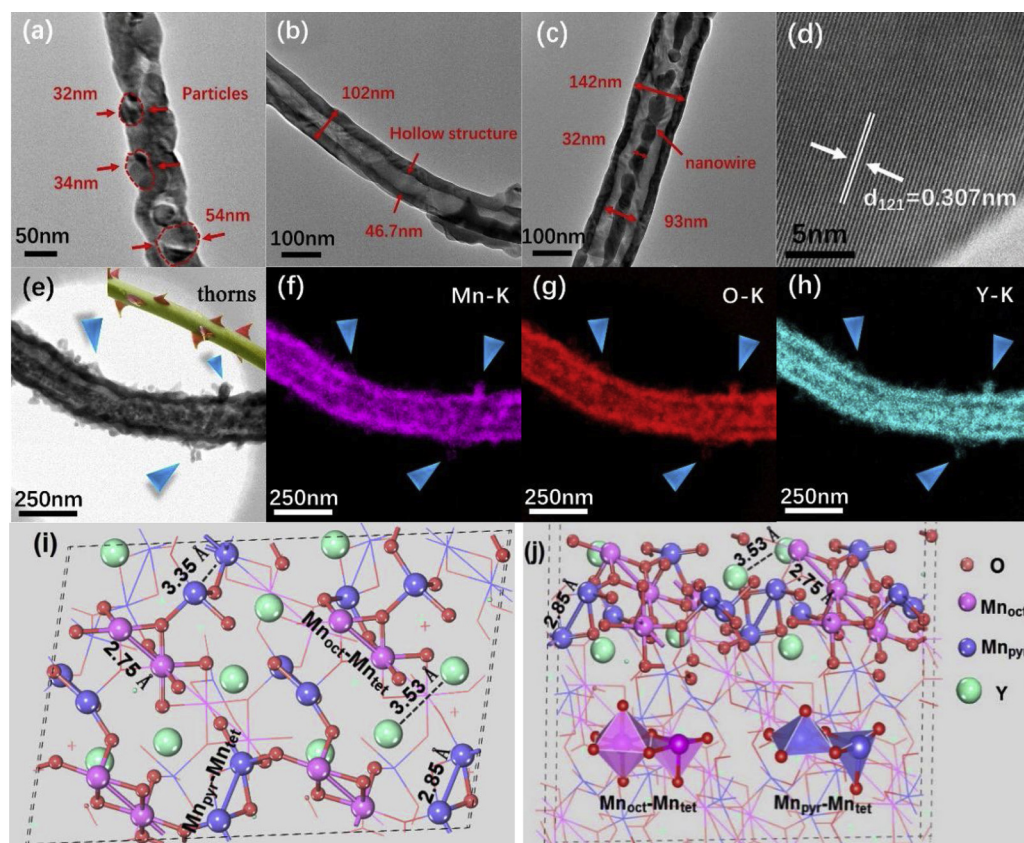
Fig. 2. TEM images (a, b, c) of YMO nanofibers and (d) the corresponding HRTEM image; STEM image (e) and (f–h) elemental maps of Mn, O and Y of the mullite fibers; Top view (i) and side view (j) of the (2*1) supercell of Mn-mullite YMn_2O_5 (121) slab surface. The oxygen atoms, pyramidal manganese atoms, octahedral manganese atoms and yttrium atoms are labeled as red, light blue, light purple and green, respectively (For interpretation of the references to colour in this figure legend, the reader is referred to the web version of this article).

electronic states near the Fermi level are dominated by Mn $3d$ orbital (Fig. 3c). The local density of states of the surface Mn-Mn dimers shows that two types of Mn atoms both contribute to the valence band maximum (Fig. 3d). Therefore, e_g orbitals (d_{z2} and d_{x2-y2}) in the Mn^{4+}-centered octahedron could be occupied as well, as shown in Fig. 3d and Fig. S6, resulting in strengthening the interaction between catalyst surface and the incoming O_2 molecules, which is beneficial to activate O−O bonds (Fig. S7). Therefore, in contrast to powder-based mullite oxide [20,27], the fiber could be potentially more promising to display higher catalytic performance owing to the larger amount of active sites.
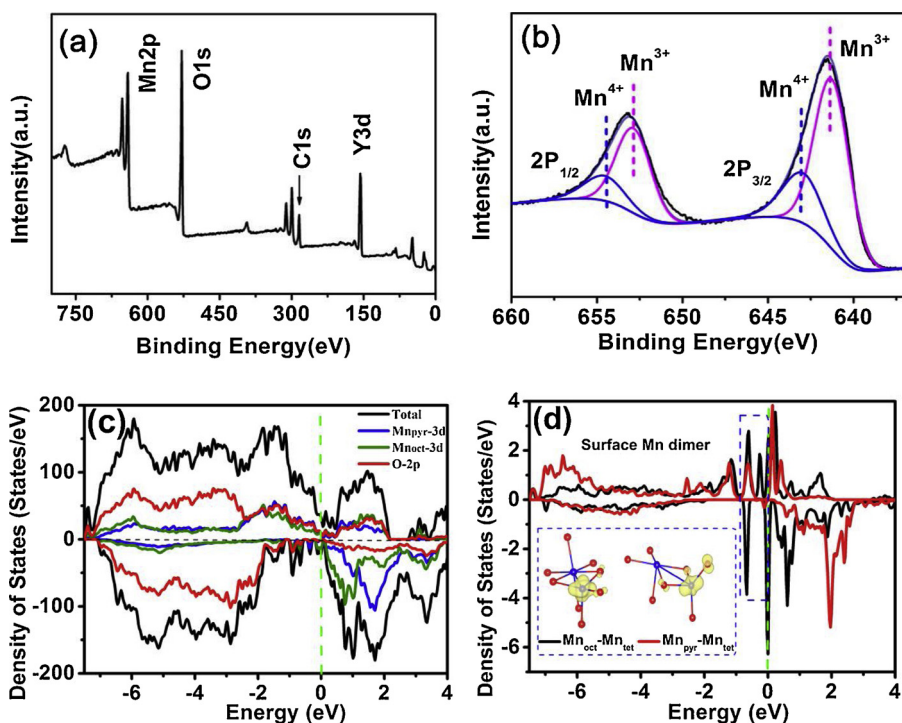
Fig. 3. XPS spectra of the YMn_2O_5 nanofibers: (a) survey spectra, (b) Mn-2p spectra; (c) the calculated total, Mn_{pyr}-3d, Mn_{oct}-3d and O-2p orbital-projected density of states of YMn_2O_5 (121) slab surface; (d) the local density of states of surface Mn dimers of YMn_2O_5 (121) slab surface and the partial charge density of the occupied orbitals below the Fermi level 0.89 eV of Mn_{oct}-Mn_{tet} and Mn_{pyr}-Mn_{tet} of YMn_2O_5 (121) slab surface (isosurface = 0.04 e/Å^3); Fermi level is set at zero energy. The oxygen and manganese yttrium atoms are labeled as red and blue, respectively. (For interpretation of the references to colour in this figure legend, the reader is referred to the web version of this article).
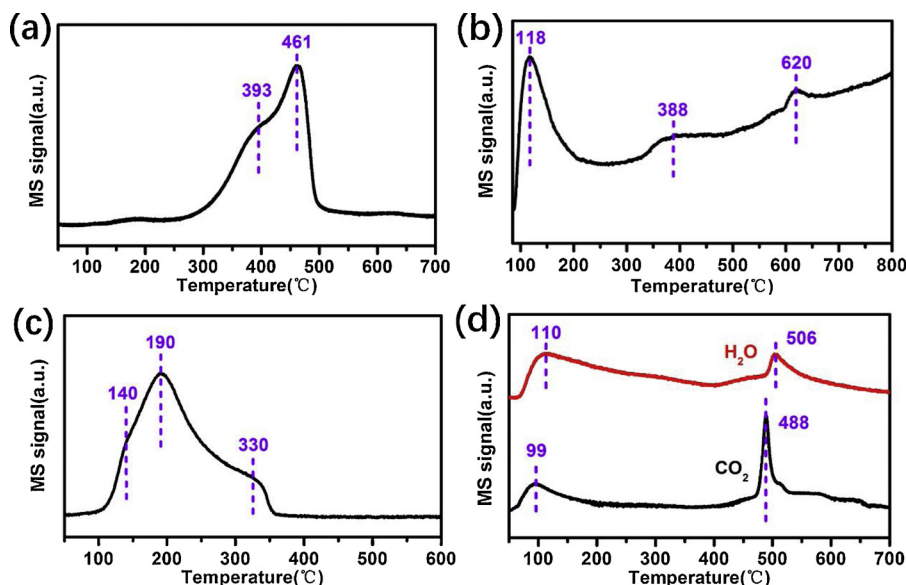
Fig. 4. (a) H_2-TPR (b) O_2-TPD (c) NO-TPD and (d) CO_2-TPD profiles of YMn_2O_5 nanofibers measured by Mass Spectrometer.

3.3. TPR and TPD analysis

H_2-TPR profiles of YMO samples were conducted to investigate the relative reducibility. Two reduction peaks were detected as shown in Fig. 4a. The first reduction peak at 393 °C is correlated to the removal of surface O_{ads} as the adsorbed oxygen molecules are easily dissociated on the surface of the mullite [20]. The second peak at 461 °C was assigned to the reduction of Mn^{4+} to Mn^{3+} [35,36]. The amount of H_2 consumed reflects the amount of thermal desorption of oxygen on the sample to some extent, which is consistent with the following result of O_2-TPD. Besides, the central position of the reduction peaks for YMO are slightly shifted to lower temperatures than those of reported Mn-La and Mn-Cu oxides [37,38], indicating that the mullite fibers are easily reduced.

To understand the O_2 and NO desorption and subsequently access the NO oxidation mechanism, the O_2-TPD and NO-TPD spectra of YMO catalyst were measured in Fig. 4b and c. According to the previous literature [39], a large amount of O_2 desorbed from YMO catalyst at T <250 QUOTE °C °C, denoted as α-O_2 and ascribed to the physically adsorbed oxygen species which weakly bound to the surface of the catalyst. The second desorption peak denoted as β-O_2 which desorbed in the 300–50 QUOTE °C °C range. The β-O_2 could be related to surface non-stoichiometric oxygen desorption and reduction of Mn^{4+} to Mn^{3+} [40]. For the high-temperature species, named γ-O_2, desorbed at T >600 QUOTE °C °C. The γ-O_2 could correspond to the reduction of Mn^{3+} to Mn^{2+}. In this work, three O_2 desorption peaks at 118 QUOTE °C °C, 388 °C and 620 °C can be observed, respectively, as shown in Fig. 4b. Compared with the previous reports [39,40] on the powder based catalyst, we noted that the O_2 desorption temperature of YMO catalyst as a whole shifted to the low-temperature region, indicating that catalyst of YMO nanofibers possesses better low-temperature activity stemming from the special nano-fiber structure. In fact, based on previous theoretical work [21], the adsorbed O_2 could be readily decomposed into atomic O* which subsequently form chemical bonds with the surface, corresponding the O_2 desorption in 388 °C. Therefore, the large amount of low-temperature O_2 adsorption is beneficial for the O_2 conversion into O*, leading to the low-temperature catalytic NO oxidation.

For the NO-TPD patterns, an intense peak at 190 °C and two overlapping shoulders near 140 °C and 330 °C are displayed as shown in Fig. 4c. NO physically desorption peak occurs at 140 °C. The maximum NO desorption peak is at 190 °C, relating to weakly bound to the surface of the catalyst. We considered the third desorption peak (~360 °C) was

produced by the decomposition of nitrate and nitrite on the surface of the catalyst. Similar to O-TPD spectrum, the main desorption process appeared in the low temperature, indicating that the YMO nanofibers catalyst has an ability to store NO at low temperature, which is very beneficial to the low-temperature catalytic reaction.

TPD-CO_2 experiments were carried out to characterize the basicity of the catalyst. Because carbon dioxide is acidic, it is expected to absorb more strongly on the basic sites. Based on previous studies [41], CO_2 may form hydrated carbonate-like species on the catalyst surface, therefore, the desorption peak of CO_2 and H_2O is simultaneously detected by mass spectrometry as shown in Fig. 4d. Two different CO_2 desorption peaks (at 100 °C and 488 °C) can be observed. The low-temperature peak (< 200 °C) likely associated to the physisorption and, the higher temperature sharp peak due to decomposition of carbonate-like species. Interestingly, by detecting the H_2O desorption peak, a similar pattern is recorded, except that the desorption temperature was slightly delayed. Similarly, we attribute the first peak to adsorbed H_2O and the higher temperature peak (at 506 °C) is attributed to hydrated carbonate-like species. Combined with O_2-TPD and CO_2-TPD analysis, it can be found that YMO NF displays oxygen storage capacity and basic sites, which may be the reason for the excellent low-temperature catalytic performance of YMO NFs.

3.4. Catalytic activity for NO oxidation

For lean-burned vehicles, to survive a high lifetime of ~200,000 km, a harsh hydrothermal aging experiment at 800 °C for 10 h with 10% water stream is required to evaluate catalyst lifetime. In order to examine the catalytic activity of the NO oxidation, the YMO-NFs, YMO-NPs, and 1.0 wt.% Pt loaded on γ-Al_2O_3 were employed to do the NO conversion in the same condition (500 ppm NO, 5% H_2O, the weight hourly space velocity (WHSV) of around 4.0 ml $min^{-1} mg^{-1}$). As shown in Fig. 5a, electrospun fibers exhibit a higher catalytic activity than hydrothermally synthesized powder-based mullite before and after aging. Specifically, the highest conversion of YMO nanofibers at 310 °C is ~18% higher than powder-based YMO at 352 °C. It is worth noting that the catalytic activity of YMO-NFs and YMO-NPs slightly reduces after aging, indicating reasonable hydrothermal stability. And the changes of their activation energy are minor (YMO-NFs: from 61.68 kJ/mol (fresh) to 77.4 kJ/mol (aged); YMO-NPs: from 91.45 kJ/mol (fresh) to 98.02 kJ/mol (aged)) as shown in Fig. 5b.

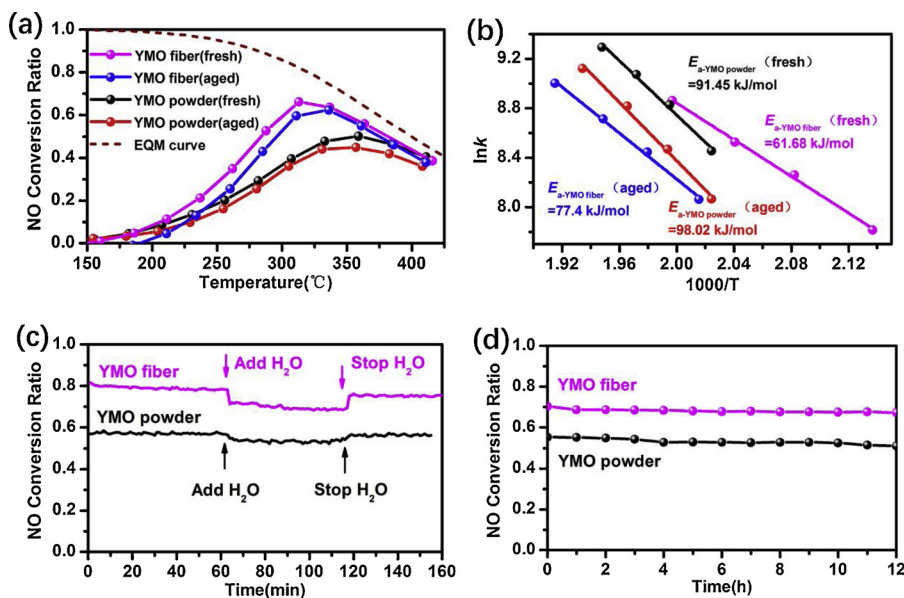In addition, we compared the NO oxidation of a Pt- powder-based

Fig. 5. (a) NO conversion as a function of reaction temperature on YMn_2O_5 fiber and powder catalysts before and after aging with $[H_2O] = 5\%$, $[O_2] = 10\%$ and $[NO] = 500\,ppm$ balanced with nitrogen at a WHSV of $240,000\,ml\,g^{-1}\,h^{-1}$. (b) The Arrhenius equation to calculate the activation energy (E_a) of fiber and powder-based mullite before and after aging within the conversion ratio below 20%. (c) The effect of steam on NO oxidation of fiber and powder-based mullite catalysts. (d) Durability test for the YMn_2O_5 fiber (at ca. 310 °C) and powder (at ca. 350 °C).

catalyst with a powder-based YMO as shown in Fig. S8a, found that the NO oxidation performance of fresh mullite powder is inferior to the Pt catalyst in the low-temperature range. However, YMO powder catalyst shows higher catalytic activity than Pt after hydrothermal aging. Meanwhile, we also compared the catalytic activities between electro-spun YMO fibers and Pt (Fig. S8b). For the fresh samples, the T_{20} (temperature at 20% NO conversion) of YMO-NFs (pink line) is only 15 °C higher than that of Pt (blue line), reversely, the highest conversion of YMO-NFs at 310 °C is ~18% higher than Pt at 340 °C. The catalytic activity of YMO nanofibers might be due to more active sites provided by the super thin nano-belts and hollow fibers with inside nanowire (see Fig. 2c). Moreover, the high Mn^{3+}/Mn^{4+} ratio also leads to the higher utilization of the Mn active sites in the octahedron (see details in XPS section). For the Pt catalyst, the T_{20} increases 50 °C with a maximum conversion of 40% at 350 °C after aging. In contrast to Pt, the fiber's T_{20} only increases by 15 °C with a maximum conversion of 62% at 335 °C. The corresponding activation energy (Fig. S8c) displays the similar catalytic performance for fresh YMO-NFs (61.68 kJ/mol) and Pt (79.48 kJ/mol), which is consistent with the reported results [42–44]. After aging, the E_a of YMO-NFs and Pt increased to 77.4 kJ/mol and 84.8 kJ/mol, respectively. We attribute the remarkable NO oxidation performance of YMO to the superior morphological stability of YMO fibers. As we discussed in the structural characterization, the tube-shaped structure could host the reaction both inside and outside the tubes. In other words, the active sites amount double in the hollow tube structure in contrast to the hydrothermally synthesized nanoparticles.

In order to explore the effect of moisture during the catalytic reaction, YMO-NFs, YMO-NPs and Pt catalysts exposure to moisture (5% H_2O) at the temperature point where their respective conversion rates are highest as shown in Fig. 5c, Fig. S9a. After the introduction of water steam, the NO conversion of both YMO-NFs and Pt decreased by ~10%, while YMO-NPs only decreased by ~4%. When stopping the stream, the performance of YMO-NFs could fully recover. In contrast, YMO-NPs and Pt approximately loose ~2% and ~6% of the activity, respectively. The performance decreases of YMO-NPs and Pt might result from the mullite and Pt powder sintering agglomeration, during which the number of active sites exposed on the powder catalyst surface is decreased. For mullite nanofibers, the superior hydrothermal robustness stems from the superstability of the fiber structures in the presence of H_2O. In addition, to explore the durability of the YMO-NFs, YMO-NPs and Pt catalyst, the NO conversion which displays the highest catalytic activity, as a function of reaction time was illustrated in Fig. 5d and Fig. S9b. It is noted that the catalytic behavior of YMO-NFs barely changed

after a 12 h continuous hydrothermal reaction. Together, the high performance, long durability, and hydrothermal stability enable YMO to be applied in the development of the next generation of the fiber catalyst based monolith converter in the after treatment of the diesel vehicles.

3.5. In situ DRIFT study

To further investigate the NO oxidation reaction mechanism over YMO catalyst, the in situ DRIFT was performed at the different temperature. NO adsorption on YMO nanofibers was investigated first by the DRIFTS at 175 °C, and the spectra are shown in the upper half of Fig. 6a. Density functional theory calculations (Table S1) were also carried out to determine the wave-numbers of gas and adsorbed nitrosyl (NO), nitrite (NO_2), and nitrate (NO_3) species on the exposed (121) mullite surface. Several IR absorption bands at $1242\,cm^{-1}$, $1289\,cm^{-1}$, $1447\,cm^{-1}$, $1532\,cm^{-1}$, $1597\,cm^{-1}$, $1624\,cm^{-1}$, $1845\,cm^{-1}$ and $1906\,cm^{-1}$ were observed, of which Mn-based bridging monodentate nitrite ($1532\,cm^{-1}$) and bridging nitro-nitrito compounds ($1289\,cm^{-1}$) were the major species, follow by Y-based nitrite or nitrate ($1447\,cm^{-1}$) [45]. Mn-based monodentate nitrate displayed a vibration mode at $1242\,cm^{-1}$, moreover, gas-phase NO exhibited an N−O stretching vibration band at $1906\,cm^{-1}$ and $1845\,cm^{-1}$, resulting from the NO adsorbed on the catalyst surface [19]. The bands of nitrate and nitrite grew with time, indicating that NO species can react with lattice oxygen to form nitrates or nitrites that are stored on the oxide surface. When 10% O_2 is introduced with the existing NO feed gas, all above-mentioned bands associated with nitrites and nitrates ($1532\,cm^{-1}$, $1289\,cm^{-1}$, $1242\,cm^{-1}$) increased significantly (the lower parts of Fig. 6a), showing that the source of oxygen supplied to supplement the consumed lattice oxygen in the metal oxide catalysts, and then continue to react with NO to form nitrates and nitrites stored on the catalyst surface, so this is the main process of storing nitrates.

Compared to Mn-based nitrite and nitrate, Y-based nitrate or nitrite absorption peaks grow relatively slowly, implying that Mn-based nitrite and nitrate are a major NO_x species. In addition, the bands of adsorption of NO_2 molecules ($1624\,cm^{-1}$) and bidentate nitrate ($1597\,cm^{-1}$) were detected, respectively, demonstrating that parts nitrites were oxidized to nitrates when the oxygen source is sufficient and then, the nitrates were quickly decomposed to produce NO_2 and partly adsorbed on the surface of the catalyst. Obviously, all the bands' intensities decrease with rising temperature (100–250 °C), demonstrating that decomposition of nitrates and nitrites adsorbed on the catalyst surface as
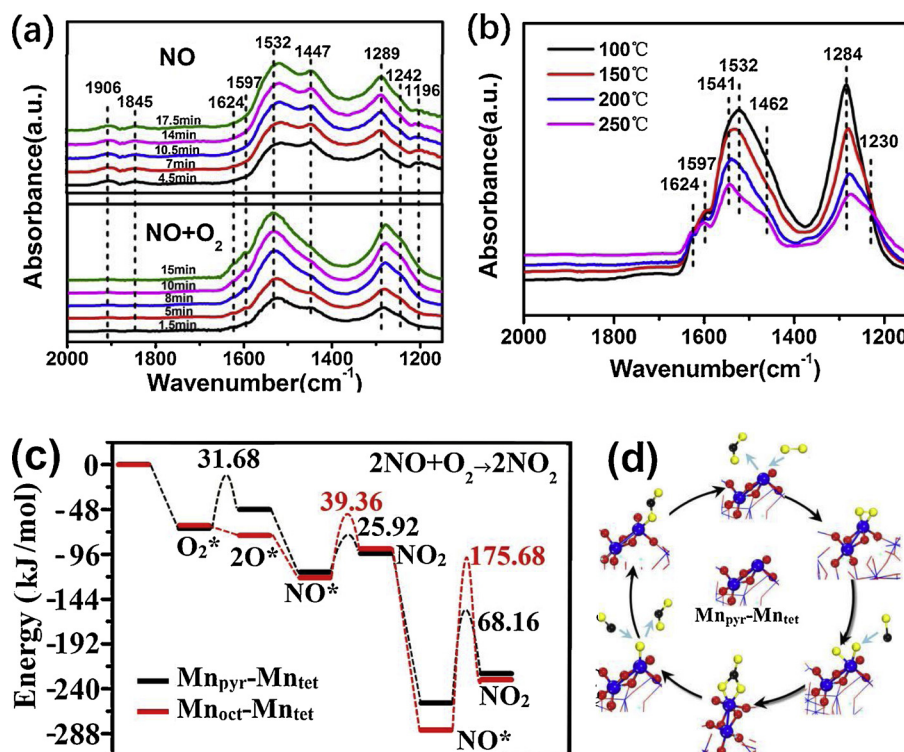
Fig. 6. In situ DRIFTS of (a) NO reacting with preadsorbed O_2 and co-adsorption of NO + O_2 over YMO at 175 °C, (b) NO + O_2 adsorption at different temperatures over YMO catalyst. (c) Energetic routes of NO oxidation on two type of active sites Mn_{pyr}-Mn_{tet} and Mn_{oct}-Mn_{tet} of (121) surface. (d) The catalytically geometrical reaction route over Mn_{pyr}-Mn_{tet}. The lattice and incoming oxygen atoms are labeled as red and yellow, respectively; the manganese and yttrium atoms are labeled as blue and green, respectively, O in gas NO and NO_2 is labeled as black (For interpretation of the references to colour in this figure legend, the reader is referred to the web version of this article).

shown in Fig. 6b. The bands of bridging monodentate nitrite ($1532 \, cm^{-1}$) and bridging nitro-nitrito compounds ($1284 \, cm^{-1}$) decreased most dramatically, implying that nitrite species were mostly consumed in the NO oxidation reaction. Interestingly, with the increase of temperature, part of the vibration peaks shifts somewhat, and the Y−O key in the bridging monodentate nitrites ($1532 \, cm^{-1}$) is interrupted to form monodentate nitrites ($1541 \, cm^{-1}$), and then further decompose to produce NO_2 release. In addition, the band at $1447 \, cm^{-1}$ (Y-based nitrites) was shifted to the band at $1462 \, cm^{-1}$ with increasing temperature and its peak became weaker, implying that partial decomposition of Y-based nitrite species. The intensity of the peaks at $1597 \, cm^{-1}$ and $1230 \, cm^{-1}$ drop was not obvious, indicating that Mn-based nitrates hardly changed than nitrites which were easy to decompose and desorption. In the whole reaction process, there are few nitrate deposits on the surface of the catalyst, most of which are the storage and decomposition of nitrite, which may be the reason for the high efficiency of the catalyst. We found that NO reacts with the lattice oxygen of the catalyst to form nitrite and nitrate which adsorbs on the surface of the catalyst. Finally, as the temperature rises, nitrite and nitrate generated are decomposed into NO_2 and released, follow the Mars-van Krevelen mechanism [46].

Upon the above identification of adsorbed NO_x species by DRIFT analyses, DFT calculations were employed to further confirm the origin of low-temperature activity and elucidate the possible reaction mechanisms on O-vacancy (121) surface. Two active sites were considered, i.e., Mn_{pyr}-Mn_{tet} and Mn_{oct}-Mn_{tet}, which both assist in activating O_2 molecules according to the above Mn-3d orbitals analysis of VBM. NO molecules prefer to adsorb on the top sites of Mn-dimes vertically (Fig. S7). O_2 molecules tend to parallelly bind with the top sites of Mn dimers. NO adsorption on the exposed Mn_{pyr}-dimes and Mn_{oct}-dimes is weaker (77.76 and 102.40 kJ/mol, respectively) than O_2 (126.72 and 252.48 kJ/mol, respectively). The complete NO oxidation reaction

route is shown in Fig. 6c, d, and Fig. S10, respectively. Over the Mn_{pyr}-dimes, O_2 molecules adsorb firstly, then it dissociates into two active oxygen atoms with the activation energy barrier of 31.68 KJ/mol. Sequentially, NO molecules react with the active oxygen atoms and form two NO_2 molecules. During the whole reaction, the desorption energy barrier of the first and second NO_2 is 25.92 and 68.16 kJ/mol, respectively. The rate-determining step can be identified as desorption of the second NO_2. In other words, the NO_3 species would not be accumulated during NO oxidation process on YMO, consistent with DRIFT experimental results (Fig. 6a). The calculated thermodynamics and dynamics activation energy barriers are both comparable with the experimental dynamic activation energy barriers from the Arrhenius equation. For the Mn_{oct}-dimers, the overall reaction route is similar to Mn_{pyr}-dimers. Due to the vacancy O existing between Y and Mn atoms, in the whole reaction process, no nitrate species are detected considering the analyses IR spectra. As a result, O_2 dissociates without energy barrier, and the first and second NO_2 desorbs with activation energy barriers of 39.36 and 175.68 kJ/mol, respectively. As a rate-determining step, the filled lattice O* between Mn and Y is more difficult to be desorbed as NO_2 molecule. Overall, NO oxidation reaction tends to occur on Mn_{pyr}-dimer sites at low temperature. Understanding the fundamentals enables to access the microscopic process of the reactions and further design more effective catalysts for various applications.

4. Conclusions

YMO nanofibers with various morphologies were fabricated by electrospinning technique and subsequently calcined at 800 °C for 4 h. Comparing with powder-based mullite and commercial 1.0 wt.% Pt catalyst, the YMO nanofibers display a superior NO catalytic activity under the condition of 5% steam at WHSV of 240,000 ml g_{cat}^{-1} hour^{-1}. Specifically, NO maximum conversion of YMO nanofibers reaches 68%

at ~310 °C in regards to 50% over YMO-NPs at 352 °C and 50% over Pt at ~340 °C. The superior NO oxidation activity could be ascribed to the variety of the unique nano-morphology including super-thin nano-belt, nano-rod, nano-tube with and without inside nanowire, etc., and a large amount of Mn^{3+} which is beneficial to the formation of oxygen vacancies on the surface of the catalyst. The activation energy of NO-to-NO_2 conversion shows comparable results among YMO-NFs (61.68 kJ/mol), YMO-NPs (91.45 kJ/mol) and Pt (68.16 kJ/mol). The proposed NO catalytic oxidation mechanism over Mn_{pyr}-Mn_{tet} active sites shows that the second NO_2 desorption is the key to the whole reaction process. Thus, mullite of the YMO fibers is promising for low-temperature oxidation to rival the Pt-powder based catalyst which might also provide insights into the design of the future fiber-based monolith converter to clean the vehicle exhaust emission.

Conflict of interest

The authors declare no competing financial interest.

Acknowledgments

Appendix A. Supplementary data

Supplementary material related to this article can be found, in the online version, at doi:https://doi.org/10.1016/j.apcatb.2019.02.005.

References

[1] L. Castoldi, R. Matarrese, S. Morandi, L. Righini, L. Lietti, New insights on the adsorption, thermal decomposition and reduction of NO_x over Pt- and Ba-based catalysts, Appl. Catal. B: Environ. 224 (2018) 249–263.

[2] Y.X. Wang, F. Kapteijn, M. Makkee, NO_x reduction in the Di-Air system over noble metal promoted ceria, Appl. Catal. B: Environ. 231 (2018) 200–212.

[3] Z.S. Zhang, B.B. Chen, X.K. Wang, L. Xu, C. Au, C. Shi, M. Crocker, NO_x storage and reduction properties of model manganese-based lean NO_x trap catalysts, Appl. Catal. B: Environ. 165 (2015) 232–244.

[4] L.J. France, Q. Yang, W. Li, Z.H. Chen, J.Y. Guang, D.W. Guo, L.F. Wang, X.H. Li, Ceria modified $FeMnO_x$-enhanced performance and sulphur resistance for low-temperature SCR of NO_x, Appl. Catal. B: Environ. 206 (2017) 203–215.

[5] D. Bhatia, R.W. McCabe, M.P. Harold, V. Balakotaiah, Experimental and kinetic study of NO oxidation on model Pt catalysts, J. Catal. 266 (2009) 106–119.

[6] X. Auvray, T. Pingel, E. Olsson, L. Olsson, The effect gas composition during thermal aging on the dispersion and NO oxidation activity over Pt/Al_2O_3 catalysts, Appl. Catal. B: Environ. 129 (2013) 517–527.

[7] S.S. Mulla, N. Chen, L. Cumaranatunge, G.E. Blau, D.Y. Zemlyanov, W.N. Delgass, W.S. Epling, F.H. Ribeiro, Reaction of NO and O_2 to NO_2 on Pt: kinetics and catalyst deactivation, J. Catal. 241 (2006) 389–399.

[8] X. Auvray, L. Olsson, Stability and activity of Pd-, Pt- and Pd-Pt catalysts supported on alumina for NO oxidation, Appl. Catal. B: Environ. 168 (2015) 342–352.

[9] L.D. Li, L.L. Qu, J. Cheng, J.J. Li, Z.P. Hao, Oxidation of nitric oxide to nitrogen dioxide over Ru catalysts, Appl. Catal. B: Environ. 88 (2009) 224–231.

[10] R.D. Zhang, A. Villanueva, H. Alamdari, S. Kaliaguine, Cu- and Pd-substituted nanoscale Fe-based perovskites for selective catalytic reduction of NO by propene, J. Catal. 237 (2006) 368–380.

[11] M. Kang, T.H. Yeon, E.D. Park, J.E. Yie, J.M. Kim, Novel MnO_x catalysts for NO reduction at low temperature with ammonia, Catal. Lett. 106 (2006) 1–2.

[12] L. Lietti, I. Nova, G. Ramis, L.D. Acqua, G. Busca, E. Giamello, P. Forzatti, F. Bregani, Characterization and reactivity of V_2O_5-MoO_3/TiO_2 De-NO_x SCR catalysts, J. Catal. 187 (1999) 419–435.

[13] A.Y. Wang, Y.L. Guo, F. Gao, C.H.F. Peden, Ambient-temperature NO oxidation over amorphous CrO_x-ZrO_2 mixed oxide catalysts: significant promoting effect of ZrO_2, Appl. Catal. B: Environ. 202 (2017) 706–714.

[14] Y. Peng, J.H. Li, X. Huang, X. Li, W.K. Su, X.X. Sun, D.Z. Wang, J.M. Hao,

[15] Deactivation mechanism of potassium on the V_2O_5/CeO_2 catalysts for SCR reaction: acidity, reducibility and adsorbed-NO_x, Environ. Sci. Technol. 48 (2014) 4515–4520.

[15] H.Z. Chang, X.Y. Chen, J.H. Li, L. Ma, C.Z. Wang, C.X. Liu, J.W. Schwank, J.M. Hao, Improvement of activity and SO_2 tolerance of Sn-modified MnO_x-CeO_2 catalysts for NH_3SCR at low temperatures, Environ. Sci. Technol. 47 (2013) 5294–5301.

[16] C.L. Zhang, S.H. Yu, Nanoparticles meet electrospinning: recent advances and future prospects, Chem. Soc. Rev. 13 (2014) 4423–4448.

[17] D. Li, Y.L. Wang, Y.N. Xia, Electrospinning of polymeric and ceramic nanofibers as uniaxially aligned arrays, Nano Lett. 3 (2003) 1167–1171.

[18] I. Moreno, N. Navascues, S. Irusta, J. Santamaria, Electrospun Au/CeO_2 nanofibers: a highly accessible low-pressure drop catalyst for preferential CO oxidation, J. Catal. 329 (2015) 479–489.

[19] W.C. Wang, G. McCool, N. Kapur, G. Yuan, B. Shan, M. Nguyen, U.M. Graham, B.H. Davis, G. Jacobs, K. Cho, X.H. Hao, Mixed-phase oxide catalyst based on Mn-mullite (Sm, Gd)Mn_2O_5 for NO oxidation in diesel exhaust, Science 337 (2012) 832–835.

[20] H.B. Li, Z. Yang, J.Y. Liu, X.L. Yao, K. Xiong, H. Liu, W.H. Wang, F. Lu, W.C. Wang, Electronic properties and native point defects of high efficient NO oxidation catalysts $SmMn_2O_5$, Appl. Phys. Lett. 109 (2016) 211903.

[21] Z.Z. Chen, X. Liu, K. Cho, R. Chen, B. Shan, Density functional theory study of the oxygen chemistry and NO oxidation mechanism on low-index surfaces of $SmMn_2O_5$ mullite, ACS Catal. 5 (2015) 4913–4926.

[22] P. Hohenberg, W. Kohn, Inhomogeneous electron gas, Phys. Rev. B 136 (1964) B864.

[23] G. Kresse, J. Hafner, Ab initio molecular-dynamics simulation of the liquid-metal-amorphous-semiconductor transition in germanium, Phys. Rev. B 49 (1994) 14251.

[24] J.P. Perdew, J.A. Chevary, S.H. Vosko, K.A. Jackson, M.R. Pederson, D.J. Singh, C. Fiolhais, Erratum: atoms, molecules, solids, and surfaces: applications of the generalized gradient approximation for exchange and correlation, Phys. Rev. B 48 (1993) 4978.

[25] J.P. Perdew, K. Burke, M. Ernzerhof, Generalized gradient approximation made simple, Phys. Rev. Lett. 77 (1996) 3865.

[26] P.E. Blöchl, Projector augmented-wave method, Phys. Rev. B 50 (1994) 17953.

[27] H.B. Li, W.H. Wang, X.Y. Qian, Y.H. Cheng, X.J. Xie, J.Y. Liu, S.H. Sun, J.G. Zhou, Y.F. Hu, J.P. Xu, L. Li, Y. Zhang, X.W. Du, K.H. Gao, Z.Q. Li, C. Zhang, S.D. Wang, H.J. Chen, Y.D. Zhao, F. Lu, W.C. Wang, H. Liu, Identifying the descriptor governing NO oxidation on mullite Sm (Y, Tb, Gd, Lu) Mn_2O_5 for diesel exhaust cleaning, Catal. Sci. Technol. 6 (2016) 3971–3975.

[28] G. Henkelman, H. Jónsson, Improved tangent estimate in the nudged elastic band method for finding minimum energy paths and saddle points, J. Chem. Phys. 113 (2000) 9978–9985.

[29] G. Henkelman, B.P. Uberuaga, H. Jónsson, A climbing image nudged elastic band method for finding saddle points and minimum energy paths, J. Chem. Phys. 113 (2000) 9901–9904.

[30] S.F. Li, H.Q. Lu, P.L. Li, Z.X. Yang, Z.X. Guo, First-principles local density approximation (generalized gradient approximation) + U study of catalytic Ce_nO_m clusters: U value differs from bulk, J. Chem. Phys. 128 (2008) 164718.

[31] S. Afzal, X. Quan, J.L. Zhang, High surface area mesoporous nanocast $LaMO_3$ (M = Mn, Fe) perovskites for efficient catalytic ozonation and an insight into probable catalytic mechanism, Appl. Catal. B: Environ. 206 (2017) 692–703.

[32] A. Machocki, T. Ioannides, B. Stasinska, W. Gac, G. Avgouropoulos, D. Delimaris, W. Grzegorczyk, S. Pasieczna, Manganese-lanthanum oxides modified with silver for the catalytic combustion of methane, J. Catal. 227 (2004) 282–296.

[33] M.R. Morales, B.P. Barbero, L.E. Cadus, Total oxidation of ethanol and propane over Mn-Cu mixed oxide catalysts, Appl. Catal. B: Environ. 67 (2006) 229–236.

[34] D. Delimaris, T. Ioannides, VOC oxidation over MnO_x-CeO_2 catalysts prepared by a combustion method, Appl. Catal. B: Environ. 84 (2008) 303–312.

[35] H.Z. Chang, J.H. Li, X.Y. Chen, L. Ma, S.J. Yang, J.W. Schwank, J.M. Hao, Effect of Sn on MnO_x-CeO_2 catalyst for SCR of NO_x by ammonia: enhancement of activity and remarkable resistance to SO_2, Catal. Commun. 27 (2012) 54–57.

[36] Z.J. Feng, J.Q. Wang, X. Liu, Y.W. Wen, R. Chen, H.F. Yin, M.Q. Shen, B. Shan, Promotional role of La addition in the NO oxidation performance of a $SmMn_2O_5$ mullite catalyst, Catal. Sci. Technol. 6 (2016) 5580–5589.

[37] A. Machocki, T. Ioannides, B. Stasinska, W. Gac, G. Avgouropoulos, D. Delimaris, W. Grzegorczyk, S. Pasieczna, Manganese-lanthanum oxides modified with silver for the catalytic combustion of methane, J. Catal. 227 (2004) 282–296.

[38] M.R. Morales, B.P. Barbero, L.E. Cadus, Total oxidation of ethanol and propane over Mn-Cu mixed oxide catalysts, Appl. Catal. B Environ. 67 (2006) 229–236.

[39] D. Fino, N. Russo, G. Saracco, V. Specchia, The role of suprafacial oxygen in some perovskites for the catalytic combustion of soot, J. Catal. 217 (2003) 367–375.

[40] Y.N. Lee, R.M. Lago, J.L.G. Fierro, V. Cortes, F. Sapina, E. Martinez, Surface properties and catalytic performance for ethane combustion of $La_{1-x}K_xMnO_{3+\delta}$ perovskites, Appl. Catal. A Gen. 207 (2001) 17–24.

[41] A. Marsal, E. Rossinyol, F. Bimbela, C. Tellez, J. Coronas, A. Cornet, J.R. Morante, Characterization of $LaOCl$ sensing materials using CO_2-TPD, XRD, TEM and XPS, Sens. Actuators B 109 (2005) 38–43.

[42] S.S. Mulla, N. Chen, W.N. Delgass, W.S. Epling, F.H. Ribeiro, NO_2 inhibits the catalytic reaction of NO and O_2 over Pt, Catal. Lett. 100 (2005) 267–270.

[43] A.A. Verma, S.A. Bates, T. Anggara, C. Paolucci, A.A. Parekh, K. Kamasamudram, A. Yezerets, J.T. Miller, W.N. Delgass, W.F. Schneider, F.H. Ribeiro, NO oxidation: a probe reaction on Cu-SSZ-13, J. Catal. 312 (2014) 179–190.

[44] B.M. Weiss, E. Iglesia, Mechanism and site requirements for NO oxidation on Pd catalysts, J. Catal. 272 (2010) 74–81.

[45] K.I. Hadjiivanov, Identification of neutral and charged N_xO_y surface species by IR spectroscopy, Catal. Rev. Sci. Eng. 42 (1&2) (2000) 71–144.

[46] C. Doornkamp, V. Ponec, The universal character of the Mars and Van Krevelen mechanism, J. Mol. Catal. A Chem. 162 (1–2) (2000) 19–32.